Journal of Hydroscience and Hydraulic Engineering
Vol. 12, No. 1, May, 1994, 1-25

NON-UNIFORM OPEN-CHANNEL FLOW OVER A ROUGH BED

By

T. Song and W. H. Graf

Laboratoire de Recherches Hydrauliques
École Polytechnique Fédérale de Lausanne, Switzerland

SYNOPSIS

Mean-flow properties and turbulence characteristics of steady non-uniform, both accelerating and decelerating, flows were experimentally studied in an open channel with a rough bed. A recently developed Acoustic Doppler Velocity Profiler (ADVP) was used to obtain instantaneously the flow profiles. From these measurements, the mean velocities, the turbulence-intensities as well as the Reynolds-stress profiles were obtained.

The flows investigated in the present study are all in equilibrium. The experimental results show that: *i*) The pressure-gradient parameter β parameterizes non-uniform flow; *ii*) The velocity distribution is given by the log-law with $B_r = 8.28 \pm 0.47$ in the inner region and by the Coles' law in the entire region, where the wake-strength parameter, Π, depends on the β-value; *iii*) The distributions of the turbulence intensities and of the Reynolds stress decrease in accelerating and increase in decelerating flow, when compared with the ones for uniform flow. Using the equations of St. Venant and the Reynolds equations, theoretical expressions for the friction velocity, vertical velocity and the Reynolds-stress distribution could be obtained, which compare favorably with the measured data.

INTRODUCTION

Non-uniform flows are often encountered in river hydraulics. Knowledge of the flow structure is of importance for sediment and pollution transport as well as for determination of the flow's resistance.

Over the past decades, the mean-flow properties and its turbulent structure of uniform open-channel flow have been extensively investigated (5). However only a few researchers studied the effect of non-uniformity on the velocity distribution and the turbulence characteristics.

Cardoso, Graf and Gust (2), using a hot-wire anemometer, studied gradually accelerating flow in a smooth channel. While very close to the bed the log-law remains valid, in the outer region Coles' law of the wake is existent. A correlation of Coles' wake parameter, Π, with a dimensionless pressure gradient, β, was proposed. The acceleration of the mean flow was accompanied by a progressive reduction (compared with uniform flow) of the turbulence intensities over the entire flow depth. However it must be noted that the flows investigated were not always in equilibrium.

Kironoto and Graf (8) investigated accelerating and decelerating flows in a rough channel. A hot-film anemometer was used to measure the velocity and turbulence profiles. The log-law explains the inner-region data and the Coles' law of the wake the outer data. Coles' wake parameter, Π, depends on the pressure-gradient parameter, β, which characterize the flow's non uniformity; an indicative relation was proposed. The turbulence intensities as well as the Reynolds stress decrease in accelerating and increase in decelerating flow when compared with the ones in uniform flow. However it must be noted, that while the flow was well in equilibrium, the experiments were limited to flow with small aspect ratios, $B/D<2.9$; implying 3-D flows.

Tsujimoto, Saito and Nitta (18) studied non-uniform flow over a short incline positioned in an open channel; all flows are not in equilibrium. Nevertheless the observed tendencies are comparable to the ones of Kironoto and Graf (8).

The present research is thus a further contribution to our understanding of the flow structure in rough non-uniform flow, using notably a recently developed instrument to measure velocities and velocity fluctuations as well as their distributions.

This research consists of two parts. Firstly, a series of experiments will be carried out to study the effect of non-uniformity on the flow properties. Then, the method for calculating the friction velocity, the vertical velocity distribution and the Reynolds stress distribution in non-uniform flow will be deduced on the basis of the St. Venant equations and the equations of Reynolds. Finally, the measured data will be compared with the theoretical formulas.

EXPERIMENTAL SET-UP AND MEASURING EQUIPMENT

Flume

A recirculating flume being 16.8 m long, 60 cm wide and 80 cm high was used, which can be tilted to slopes of $-1 < S[\%] < 9$. The flume has glass walls and a steel bottom which can be modified by adding sediment or other roughness. Several flow-stabilizing devices exist in the flume entrance to assure uniform flow conditions. The details of the flume can be found in Graf and Suszka (6). In Fig. 1 is shown the general view of the measuring section and the equipment installation. The measuring reach is situated between $5.6 < x\ [m] < 15.6$, measured from the downstream of the stabilizing devices. Within this measuring reach the flow is considered to be fully developed. The entire measuring reach was used to test flow equilibrium. Subsequently, the flow parameters at one single section at $x = 14.1$ m were investigated.

In our experiments, the flume's bed consists of gravel which has a nearly uniform diameter. The height of the gravel layer is about 10 cm. The size distribution of the gravel was analyzed with the method of Wolman, being $d_{50} = 1.23$ cm, $d_{16} = 0.90$ cm and $d_{84} = 1.65$ cm. The specific gravity is $s_s = 2.75$ and the angle of repose is $\varphi = 35^o$. By changing the bed slope and by regulating the tail gate a series of non-uniform flows could be created. Altogether this imposed on our study small aspect ratios $2.93 < B/D < 4.6$. In another investigation (16), it was found that a reasonable two-dimensional flow in the middle of the section exists, if the aspect ratio is $B/D \geq 3.5$.

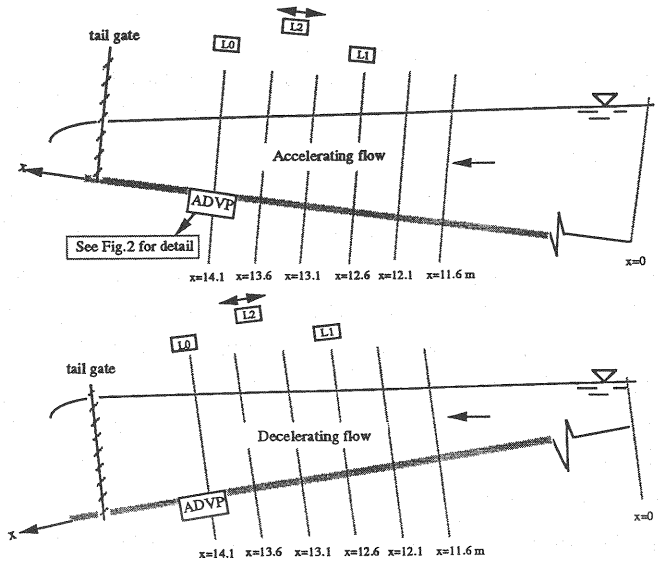

Fig. 1 General view of measuring reach.

Measuring Instruments

An *electromagnetic flow meter* was installed in the conduit connected with the flume to measure continuously the discharge passing through the channel. It was calibrated by another highly-accurate flow meter.

Two *ultrasonic limnimeters* (L0, L1) with an accuracy of 1 mm were installed at 2 different sections, at x[m] = 12.6, 14.1, to measure the flow depths and to control the non uniformity of the flow. Another one (L2) was fixed on a mobile carriage. For each experiment, this carriage was displaced between $12.6 < x[m] < 15.6$ to determine the local variation of the flow depth.

An *Acoustic Doppler Velocity Profiler (ADVP)*, developed at the LRH of EPFL, was used to measure instantaneously the distributions of velocity and of turbulence. This is a non-intrusive and direct measuring device. The details of the ADVP were presented before (9) to (12), but will be briefly described in the following.

The ADVP operates on the principle of the Doppler shift in the back scattered acoustic energy due to density inhomogeneities ("targets") moving with the water, such as density fronts resulting

from turbulent dissipation (11). Acoustic waves with the frequency f_o and speed c are emitted by a transducer and pass through a water column in which these targets move with the velocity, u and v, whose radial component, V, is oriented along the acoustic beam of the transducer (Fig. 2). Due to the targets' motion, the waves are reflected towards the transducer with a frequency f_r. The difference $f_d = (f_o - f_r)$ is called the Doppler-shift frequency, for which the following linear relationship can be given:

$$c = \xi V f_o/f_d \qquad (1)$$

where $\xi = 2$ since the moving target serves first as receiver and then as emitter. With c and f_o given, f_r is measured and the radial velocity, V, can be calculated.

The present monostatic ADVP operates in the pulse-to-pulse coherent mode to provide time series of the Doppler-shift frequency. A short train of several sinusoidal waves, the "pulse", is emitted at regular intervals (the pulse-repetition frequency - PRF). Between two emissions the transducer serves as a receiver. An electronic system detects the difference between the two frequencies and provides a signal corresponding to the instantaneous Doppler frequency, f_d. By time-gating the received signals to correspond to the pulse's time of flight to the point of interest, a sequence of a small sampling volumes (the gates) can be interrogated after each pulse, resulting in an instantaneous profile of velocity. The number of gates, the pulse-repetition frequency (PRF) and the pulse width (Δt, determining the axial dimension of the gate) are software-controlled. Most of our experiments were conducted with a 6 microsecond-pulse width and a 1000 Hz PRF (resulting in 1000 instantaneous profiles each second) using a 1 MHz acoustic frequency.

In the present experiments the ADVP was connected successively, one at a time to three transducers at positions T1, T2 and T3 (Fig. 2). Transducer T2 is directed vertically, $\alpha_2 = 0^o$, transducers T1 and T3 are tilted, $\alpha_1 = \alpha_3 = \alpha = 30^o$. The three beams intersect in a region slightly below the water surface. The "pulse-pair" method (9) was used to extract the Doppler shift frequency, f_d.

Using geometric relations (Fig. 2), the radial velocities can be expressed as components of the instantaneous point velocities of the target, u(y), v(y):

for T1: $$V_1 = u_1 \sin\alpha - v_1 \cos\alpha \qquad (2)$$

for T2: $$V_2 = -v_2 \qquad (3)$$

for T3: $$V_3 = -u_3 \sin\alpha - v_3 \cos\alpha \qquad (4)$$

The instantaneous velocities are expressed by mean values plus fluctuation components:

$$V_j = \overline{V_j} + V_j' \qquad \text{etc. for } u_j \text{ and } v_j \qquad (j = 1, 2, 3) \qquad (5)$$

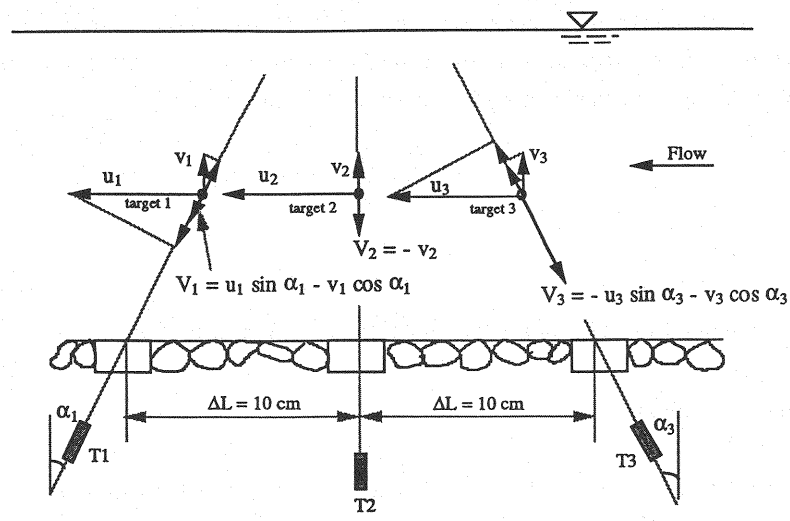

Fig. 2 Installation of the ADVP transducers and velocity decomposition

In gradually varied non-uniform flow the variation of the water depth, dD/dx, is very small. Since the distance over which the transducer measures the flow parameters was also small (being $2\Delta L$ = 0.2 m at the most), it will be considered that the hydraulic quantities in horizontal planes at the same vertical position, y, are the same:

$$\overline{u_j} \equiv \overline{u} \; ; \qquad \overline{v_j} \equiv \overline{v} \tag{6}$$

$$\overline{u_j' v_j'} \equiv \overline{u'v'} \; ; \qquad \overline{u_j'^2} \equiv \overline{u'^2} \; , \qquad \overline{v_j'^2} \equiv \overline{v'^2} \; , \tag{7}$$

Consequently the mean velocities, the covariance and the variances can be deduced:

$$\overline{u} = \frac{\overline{V_1} - \overline{V_3}}{2 \sin \alpha} \; ; \qquad \overline{v} = -\frac{\overline{V_1} + \overline{V_3}}{2 \cos \alpha} \quad [\text{ or } \quad \overline{v} = -\overline{V_2} \;]^* \tag{8); (9)}$$

$$-\overline{u'v'} = \frac{\overline{V_1'^2} - \overline{V_3'^2}}{2 \sin 2\alpha} \tag{10}$$

$$\overline{v'^2} = \overline{V_2'^2} \; ; \qquad \overline{u'^2} = \frac{\overline{V_1'^2} + \overline{V_3'^2} - 2\,\overline{V_2'^2} \cos^2 \alpha}{2 \sin^2 \alpha} \tag{11); (12)}$$

It should be remarked that the relation Eq. 9* is extremely sensitive to a precise orientation of the tilt, $\alpha_2 = 0^o$; it will not be used herein (16).

The three radial velocity profiles, $V_1(y)$, $V_2(y)$, $V_3(y)$, - this is the velocity the transducer "sees" at different depth positions (20 to 50 points, depending on the flow depth) in the flow -, were evaluated using the geometric relationships given with Eq 8 to Eq. 12, to obtain the velocity profiles, $\overline{u}(y)$, $\overline{v}(y)$, and the turbulence profiles, $\sqrt{\overline{u'^2}}$ (y), $\sqrt{\overline{v'^2}}$ (y) and $-\rho\overline{u'v'}$ (y).

The ADVP measures directly the instantaneous velocities, when a back-scattered signal is received. In turbulent flow, when inhomogeneities due to temperature gradients are encountered,

back scattering is assured. (However these signals might be disturbed by parasitic signals from the boundaries of the flow, which will give recognizable wrong velocities). The instrument was found to have an accuracy comparable or better than the hot-film anemometer.

EXPERIMENTAL RESULTS

Flow Parameters

For accelerating flow, 12 profiles and for decelerating flow, 9 profiles, of mean flow velocity, $\bar{u}(y)$ and $\bar{v}(y)$, and of turbulence, $\sqrt{\overline{u'^2}}$ (y), $\sqrt{\overline{v'^2}}$ (y) and $-\rho\overline{u'v'}$ (y), have been measured. All measurements were done at the section at x = 14.1m. The flow parameters are summarized in Table 1.

To parameterize non-uniform flow, a dimensionless longitudinal pressure-gradient parameter, β (8), will be used, defined as:

$$\beta = \frac{D}{\tau_o}\frac{dp^*}{dx} = \frac{D}{\tau_o} g\rho \left(- S + \frac{dD}{dx} \right) \qquad (13)$$

in which, D is the flow depth; τ_o is the bed-shear stress; S is the bed slope and dD/dx is the longitudinal variation of the water depth. For uniform flow, $\beta = -1$; for decelerating flow $\beta > -1$ and for accelerating one $\beta < -1$. The β-values for all runs are given in Table 1. This parameter, β, is similar to the one introduced by Clauser (4) for boundary-layer flow.

Verification of Fow Equilibrium

Before we start further investigations, it is necessary to verify if the flow within the measuring section is in equilibrium. For verification of flow equilibrium, run AS-93-Q100, being the most accelerating flow, and run DS90-Q60, being the most decelerating one, were chosen. Subsequently, it will be considered that if these two extreme runs are in equilibrium, all other runs of the present study should be also in equilibrium. For each of these runs, velocity and Reynolds-stress profiles at four sections were measured. The measured results are plotted as $\bar{u}/U_c$ and $-\overline{u'v'}/u^{*2}$ versus y/D in Fig. 3, where U_c is the maximum point velocity. From Fig. 3, it can be seen that the profiles obtained at different sections are nearly self-similar over the measuring reach.

The flow equilibrium can be further verified by using Rotta's criteria (14) written for open-channel flow as:

$$\frac{u^*}{U_c} = \text{const.} \qquad \beta = \frac{D}{\tau_o}\frac{dp^*}{dx} = \frac{D}{\tau_o} g\rho \left(- S + \frac{dD}{dx} \right) = \text{const.} \qquad (14)$$

where u^* is the friction velocity. The measured data for the two runs are plotted in Fig. 4. It is noted that the two parameters remain nearly constant over the measuring reach.

Thus it may be safely concluded that the investigated flows are in equilibrium.

Table 1 Summary of the hydraulic parameters

Run	S	Q	D	δ	B/D	U	Fr	Re	T	u^*_c	u^*	u^*_τ	B_r	Π	dD/dx	β
	%	ℓ/s	cm	cm	-	cm/s	-	(10^5)	°C	cm/s	cm/s	cm/s	-	-	-	–
Accelerating Flow																
AS00-Q145	0	145	20.0	14.12	3.00	120.83	0.86	9.99	23.2	9.24	9.30	9.70	8.0	0.210	-0.0170	-3.86
AS00-Q100	0	100	16.2	13.72	3.70	102.88	0.82	6.89	23.2	8.05	8.00	8.23	8.10	0.139	-0.0122	-3.03
AS00-Q80	0	80	14.5	12.13	4.14	91.95	0.77	5.51	23.2	7.21	7.16	7.55	8.00	0.230	-0.0090	-2.50
AS-25-Q100	-0.25	100	16.9	12.92	3.55	98.62	0.77	6.91	23.4	8.26	7.91	7.89	8.40	0.071	-0.0160	-3.58
AS-25-Q80	-0.25	80	15.1	12.13	3.97	88.30	0.73	5.52	23.4	7.36	7.28	7.36	8.22	0.064	-0.0130	-2.87
AS-25-Q60	-0.25	60	13.1	10.54	4.58	76.34	0.67	4.14	23.4	7.12	6.68	7.54	8.10	0.047	-0.0118	-2.68
AS-50-Q110	-0.50	110	17.9	12.13	3.35	102.42	0.77	7.55	22.8	7.32	7.68	8.05	8.50	0.030	-0.0200	-4.47
AS-50-Q80	-0.50	80	15.9	12.13	3.77	83.86	0.67	5.49	22.8	6.86	6.90	6.85	8.10	0.055	-0.0146	-3.15
AS-75-Q100	-0.75	100	18.2	11.73	3.30	91.58	0.69	6.91	23.4	7.45	7.20	7.42	8.10	0.131	-0.0200	-4.31
AS-75-Q80	-0.75	80	16.5	11.73	3.64	80.81	0.64	5.52	23.4	6.54	6.46	7.17	8.18	0.130	-0.0170	-3.69
AS-93-Q100	-0.93	100	19.0	12.13	3.16	87.72	0.64	6.91	23.5	7.14	6.85	6.52	8.24	0.157	-0.0205	-4.45
AS-93-Q80	-0.93	80	17.2	11.33	3.49	77.52	0.60	5.53	23.5	6.96	6.30	6.80	8.46	0.059	-0.0189	-4.08
Decelerating Flow																
Run	S	Q	D	δ	B/D	U	Fr	Re	T	u^*_c	u^*	u^*_τ	B_r	Π	dD/dx	β
	%	ℓ/s	cm	cm	-	cm/s	-	(10^5)	°C	cm/s	cm/s	cm/s	-	-	-	–
DS25-Q90	0.25	90	20.0	20.0	3.00	75.00	0.54	6.23	23.6	5.19	5.12	4.95	8.22	0.177	0.0016	-0.69
DS25-Q70	0.25	70	16.0	16.0	3.75	72.92	0.58	4.84	23.6	5.07	5.04	4.72	8.67	0.376	0.0013	-0.71
DS50-Q90	0.50	90	18.5	18.5	3.24	81.08	0.60	6.21	23.4	6.84	6.91	6.54	8.18	0.303	0.0038	-0.456
DS50-Q70	0.50	70	16.5	16.5	3.64	70.71	0.56	4.84	23.5	6.20	5.86	6.28	8.10	0.459	0.0038	-0.566
DS50-Q55	0.50	55	14.5	14.5	4.14	63.22	0.53	3.80	23.5	5.68	5.20	5.53	8.00	0.325	0.0038	-0.631
DS75-Q80	0.75	80	20.5	20.5	2.93	65.04	0.46	5.52	23.4	5.04	4.95	5.07	8.12	0.396	0.0079	0.330
DS75-Q60	0.75	60	17.0	17.0	3.53	58.82	0.46	4.14	23.4	4.96	4.91	4.97	8.70	0.447	0.0076	0.070
DS90-Q80	0.90	80	18.0	18.0	3.33	74.07	0.56	5.52	23.4	6.58	6.42	6.52	8.75	0.579	0.0095	0.214
DS90-Q70	0.90	70	18.0	18.0	3.33	64.81	0.49	4.84	23.5	5.45	5.30	5.36	8.51	0.445	0.0096	0.377

S - bed slope; Q - flow discharge; D - flow depth; δ - distance between the gravel bed and the point where $\bar{u} = U_c$; U_c - maximum point velocity; B/D - aspect ratio; $U = Q/DB$ - cross-sectional average velocity; B - flume width (60 cm); $Fr = U/\sqrt{gD}$ - Froude number; g - gravitational acceleration; $Re = 4DU/\upsilon$ - Reynolds number; υ - kinematic viscosity of water; T - water temperature; $u^*_c = \sqrt{gD[S - \frac{dD}{dx}(1 - Fr^2)]}$ - friction velocity, calculated with St. Venant's equation, Eq.(26); u^* - friction velocity, obtained from the measured velocity profile in inner region (Clauser's method); u^*_τ - friction velocity, calculated from measured Reynolds-stress profile (polynomial regression); B_r - constant of integration in log-law; Π - Cole's wake parameter; dD/dx - local variation of the water depth; β - dimensionless longitudinal pressure-gradient parameter, Eq (13).

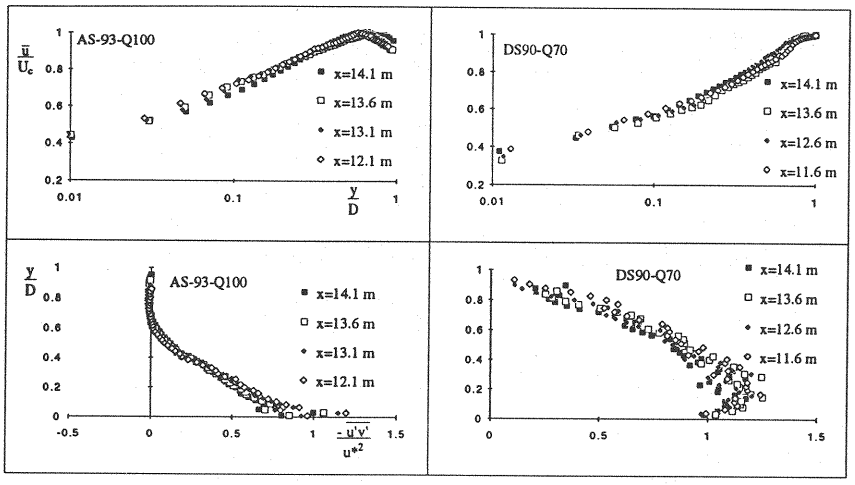

Fig. 3 Velocity and Reynolds-stress distribution at different sections

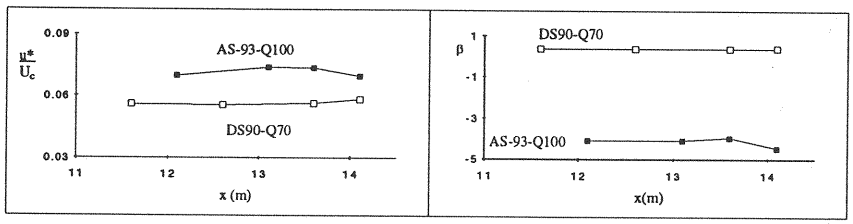

Fig. 4 Equilibrium parameters at different sections.

Horizontal Mean-Velocity Distribution

Measured Velocity Profiles

Since the flows investigated here are in equilibrium, we will only measure and exploit the data obtained at the section at x = 14.1 m. The velocity distributions, $\bar{u}(y)$, are calculated from the measured radial velocities, using Eq. 8.

In Fig. 5 is shown a comparison of velocity profiles of the most accelerating flow, AS-93-Q100, and of the most decelerating one, DS90-Q70. We can see that the profile of the accelerating flow is fuller than the one of the decelerating flow. Since these two extreme runs have different flow depth, it is difficult to say if the difference in the velocity profiles is caused by a different pressure gradient. Therefore we selected another two runs for which the flow depth is the same, D = 20 cm. The measured velocity profiles are presented also in Fig. 5. The same conclusion is obtained.

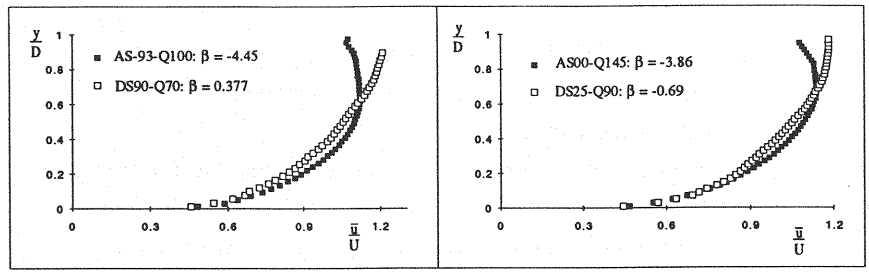

Fig. 5 Comparison of velocity profiles in accelerating flow and decelerating flows

It is also to be noted that for accelerating flows, $\beta < -1$, the maximum point velocity, U_c, is under the water surface at $y = \delta < D$. For decelerating flows, $\beta > -1$, the maximum point velocity , U_c, occurred at the water surface at $y = \delta = D$.

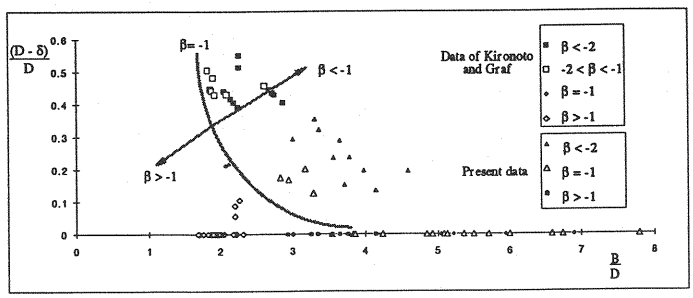

Fig. 6 Dip value versus aspect ratio

An attempt to parameterize the dip value:

$$\frac{D - \delta}{D} = f\left(\frac{B}{D}, \beta\right) \tag{15}$$

was done in Fig. 6; D is the entire flow depth and δ is the water depth at $\bar{u} = U_c$. (The present data has been supplemented by data of Kironoto and Graf, (8)). For rough uniform flow, $\beta = -1$, the aspect ratio is used to delimit, with $B/D \approx 3.5$, the 2-D and 3-D flows. If the dip value can be used as a criteria, it implies that decelerating flow, $\beta > -1$, is readily 2-D flow, while accelerating flow, $\beta < -1$, is usually 3-D flow.

Velocity Distribution in the Inner Region

For uniform and modest non-uniform open-channel flow, the velocity profile in the inner region, limited by $y/D \leq 0.20$, can be expressed by the log-law (5):

$$\frac{\bar{u}}{u^*} = \frac{1}{\kappa} \ln \frac{y + y_o}{k_s} + B_r \tag{16}$$

where $\kappa = 0.4$ is Karman's constant; u^* is the friction velocity; $\bar{u}$ is the point velocity; y is the distance from the bed; k_s is the equivalent sand roughness being equal to $k_s = d_{50} = 1.23$ cm since the gravel used in the present study is nearly uniform (3); y_o is the reference bed level; $y_o = (-) 0.25k_s$ (5) and B_r is a constant of integration.

The measured velocity profiles were plotted as $\bar{u}$ versus $(y + y_o)/k_s$. It is found that this relation was linear in the inner region for all runs, having a correlation coefficient of $R \geq 0.99$. Subsequently the values of B_r and u^* can be calculated; they are listed in Table 1.

Comparison of selected measured velocity profiles and the log-law is given in Fig. 7 where the log-law is plotted as a dashed line. It is seen that the measured velocity profiles agree well with the log-law in the inner region. For all runs, the B_r-values was nearly constant, $B_r = 8.28 \pm 0.47$, and are comparable with the values for uniform and modest non-uniform flows reported in the literature (5). Fig. 8 shows that the B_r-values are essentially independent from the pressure-gradient parameter, β.

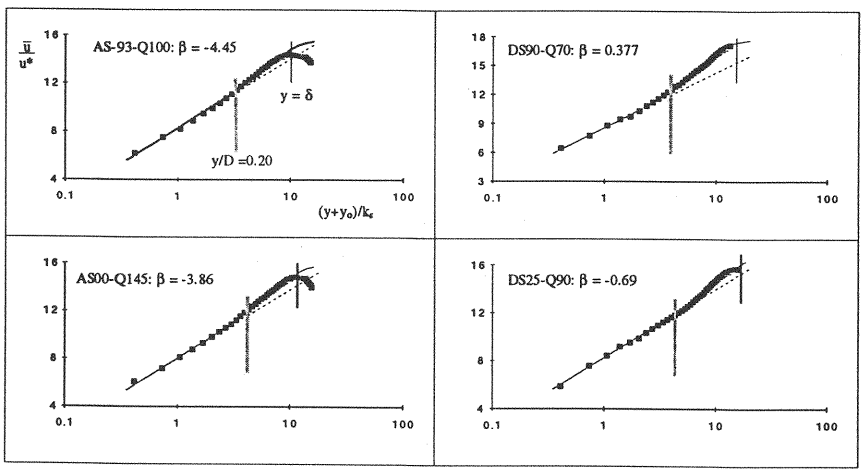

Fig. 7 Comparison of the log-law, the Coles' law and the measured velocity distribution

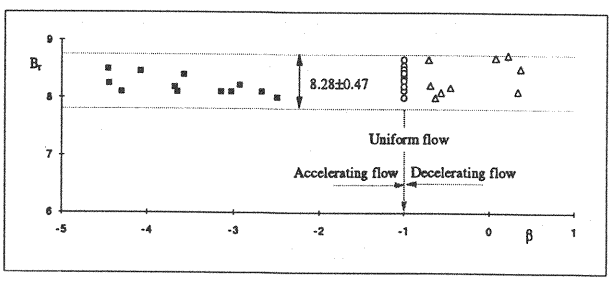

Fig. 8 Constant of integration, B_r, versus pressure-gradient parameter, β

Velocity Distribution in the Outer Region

In the outer region (but also in the inner region) the defect or wake law describes the velocity distribution. A particular form of the wake law was given by Nezu and Rodi (13) as:

$$\frac{\bar{u}}{u*} = \frac{1}{\kappa} \ln \frac{y + y_o}{k_s} + B_r + \frac{2\Pi}{\kappa} \sin^2\left(\frac{\pi (y + y_o)}{2(\delta + y_o)}\right) \qquad (17)$$

in which, δ is the distance between the bed (top of gravel) and the point where $\bar{u} = U_c$; Π is the wake-strength parameter.

The use of the wake law consists of two steps. At first, we use the log-law for calculating values of u* and B_r. Then, using these values as well as the measured velocity profiles, the wake-strength parameter, Π, was determined by iteration using Eq. 17 .

Typical measured velocity profiles are shown in Fig. 7, where the Coles' wake law is drawn as a solid line. It is noted that the measured velocity distributions coincide reasonably well with the wake law both in inner and outer region for $y < \delta$.

The wake-strength parameter, Π, depends notably on the longitudinal pressure-gradient parameter, β (5); this relationship is plotted in Fig. 9. The relation obtained by Kironoto and Graf (8) for the non-uniform flows with small aspect ratio B/D = 2 is also drawn as a dashed line. It is evident that all of our data fall above this line. As Kironoto and Graf (8) have noted, the Π-parameter depends not only on the pressure-gradient parameter, β, but also on the aspect ratio, B/D. In the present study, the aspect ratios are $2.93 < B/D < 4.58$, being thus larger than B/D = 2. The present data have been plotted in Fig. 9; it is seen that a reasonable fit is given by the empirical expression:

$$\Pi \equiv 0.088\,\beta + 0.33 \qquad (18)$$

valid for modest aspect ratios.

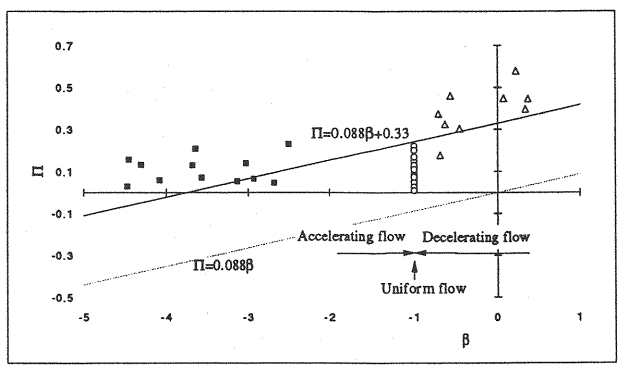

Fig. 9 Wake-strength parameter, Π, versus pressure-gradient parameter, β

Vertical Mean-Velocity Distribution

The vertical velocity distribution, $\overline{v}(y)$, are calculated from the measured radial velocity, using Eq. 9. The selected measured vertical velocity profiles are shown in Fig 10. It can be seen that the mean vertical point velocity is very small ($\overline{v} \approx 1$ cm/s) compared to the mean horizontal velocity ($\overline{u} \approx 80$ cm/s). In accelerating flows, the velocities are negative, while in decelerating flows, they are positive. This is in agreement with equation of continuity:

$$\frac{\partial \overline{u}}{\partial x} = -\frac{\partial \overline{v}}{\partial y} \tag{19}$$

We observe that for accelerating flow, $\partial\overline{u}/\partial x > 0$, and $\partial(-\overline{v})/\partial y > 0$; for decelerating flow, $\partial\overline{u}/\partial x < 0$ and $\partial(\overline{v})/\partial y > 0$. These tendencies are in qualitative agreement with the measurement shown in Fig. 10.

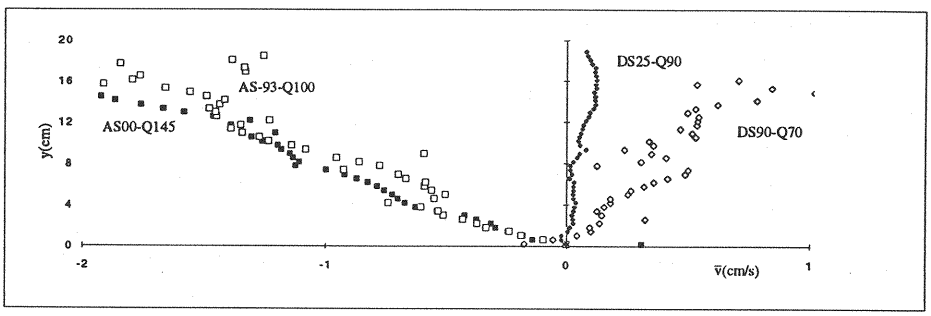

Fig. 10 Typical measured vertical velocity profiles

Turbulence-Intensity Profiles

The RMS distributions, $\sqrt{\overline{u'^2}}$ and $\sqrt{\overline{v'^2}}$, are calculated from the measured radial velocities, using Eqs. 11 and 12. Fig. 11 shows the measured $\sqrt{\overline{u'^2}}$-profiles of the selected runs. It is noted that for both accelerating and decelerating flows, $\sqrt{\overline{u'^2}}$ decreases with the depth increasing, falling to a minimum at $y = \delta$. Its maximum appears either at or close to the bed. For accelerating flow, $\sqrt{\overline{u'^2}}$ remains nearly constant, when $y > \delta$.

Fig. 12 shows the measured $\sqrt{\overline{v'^2}}$-profiles of the same selected runs. The overall tendency is the same as for the $\sqrt{\overline{u'^2}}$-profile. However slightly above the bed, the maximum values are noticed, while towards the bed the values decrease noticeably. This phenomena has been observed already for uniform flows (15).

The longitudinal and vertical components of the turbulence intensity for 6 selected runs (scaled with u*), are plotted against a distance measured from the bed (scaled with δ) in Fig. 13.

Turbulence-intensity distributions for rough uniform flow (8), (16), are plotted in the same figure for sake of comparison. The following conclusions may be drawn:

For *accelerating flow* ($\beta < -1$), the turbulence intensities are smaller than the one in uniform flow ($\beta = -1$).They have maximum values close to the bed and diminish gradually towards the point of $y = \delta$. The smaller the value of β (the more accelerating the flow), the larger is the difference to the uniform value; the turbulence profiles have a concave form.

For *decelerating flow* ($\beta > -1$), the turbulence intensities are larger than the one in uniform flow. They have a maximum at a certain distance above the bed and decrease gradually towards to the water surface. The larger the value of β (the more decelerating the flow), the larger is the difference to the uniform value; the turbulence profiles have a convex form.

Above observations are also in agreement with observations of Kironoto and Graf (8) for open-channel flow and are in qualitative agreement with Bradshaw (1) and Coleman et al. (4) for boundary-layer flow.

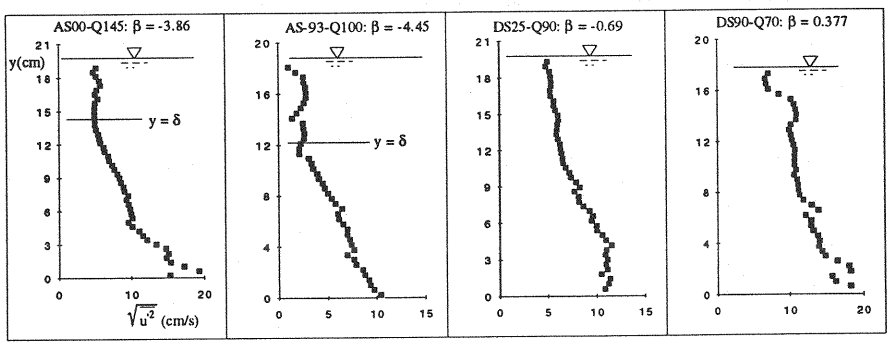

Fig. 11 Typical measured $\sqrt{u'^2}$-profiles in non-uniform flow

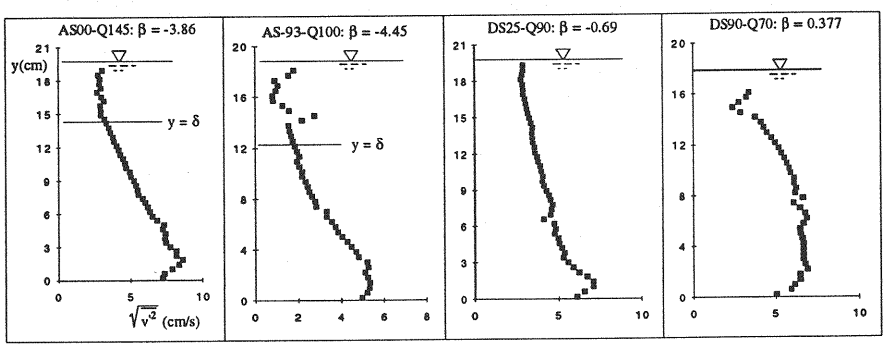

Fig. 12 Typical measured $\sqrt{v'^2}$-profiles in non-uniform flow

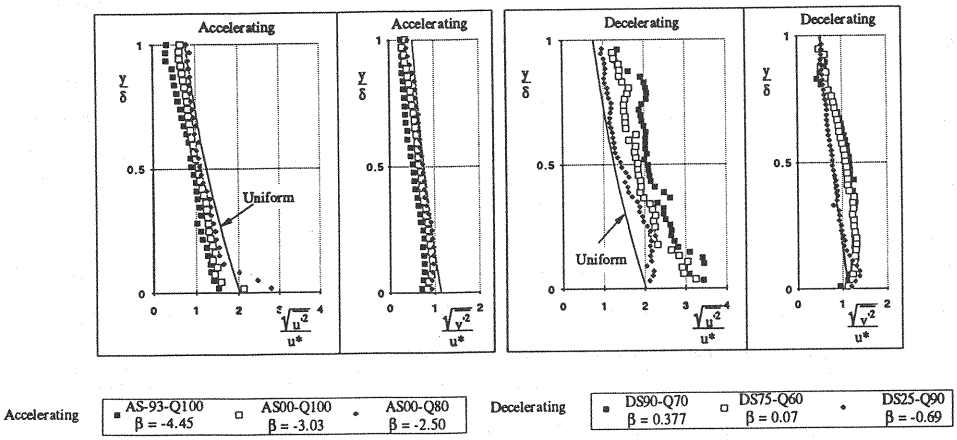

Fig. 13 Turbulence-intensity distributions for non-uniform flow

Turbulence-intensity distributions are usually (13) expressed by:

$$\frac{\sqrt{\overline{u'^2}}}{u^*} = D_u(\beta)\exp(-\lambda_u(\beta)\, y/\delta)\,; \qquad \frac{\sqrt{\overline{v'^2}}}{u^*} = D_v(\beta)\exp(-\lambda_v(\beta)\, y/\delta) \tag{20}$$

The experimental constants for rough uniform open-channel flow (8), (15) are given as:

$$D_u = 2.04,\ \lambda_u = 0.97\,; \qquad D_v = 1.14,\ \lambda_v = 0.76 \tag{21}$$

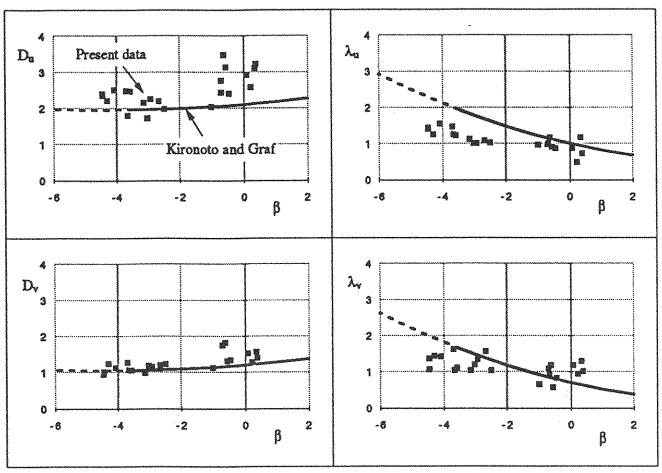

Fig. 14 Relationship between the constants D_u, D_v, λ_u, λ_v in Eq. 20 and the pressure-gradient parameter, β

For non-uniform flow, these constants depend on the pressure-gradient parameter, β. For all measured turbulence profiles, these constants have been evaluated using Eq. 20; they are plotted in Fig. 14. The present data set shows a tendency, which is similar to the one proposed by Kironoto and Graf (8). The difference between the present data and the ones of Kironoto and Graf (8) may be due to the difference in the bed roughness and of aspect ratio.

Reynolds-Stress Profiles

The measured Reynolds-stress profiles of the 6 selected runs are plotted in Fig. 15. For accelerating flow, the distributions have a concave form. The maximum values are close to the bed. At the point $y = \delta$, the Reynolds stress is zero; in the region $y > \delta$, they become negative, but absolute values are very small. For decelerating flow, the Reynolds-stress distributions become convex, having their minimum values at the water surface. Different from uniform and accelerating flows, the maximum values occur clearly above the bed.

The dimensionless Reynolds-stress distributions are also shown in Fig. 15. Adimensionalisation was obtained by using the friction velocity, u*, calculated with the Clauser method. The theoretical (linear) distribution for uniform flow is also plotted for sake of comparison. The following conclusions may be drawn:

For *accelerating flows* ($\beta < -1$), the dimensionless Reynolds-stress distributions have a concave form, falling below the curve for uniform flow. The smaller the β-value, the larger is the difference between the measured dimensionless Reynolds stress and the uniform flow value.

For *decelerating flows* ($\beta > -1$), the dimensionless Reynolds-stress distributions are convex. At a given vertical position, y/δ, the dimensionless Reynolds stress is larger than the one of uniform flow. The more decelerating the flow, the larger is the difference.

Above observations are also in agreement with observations of Kironoto and Graf (8) for open-channel flow and in qualitative agreement with Herring and Norbury (7), Bradshaw (1) and Coleman et al. (4) for boundary-layer flow.

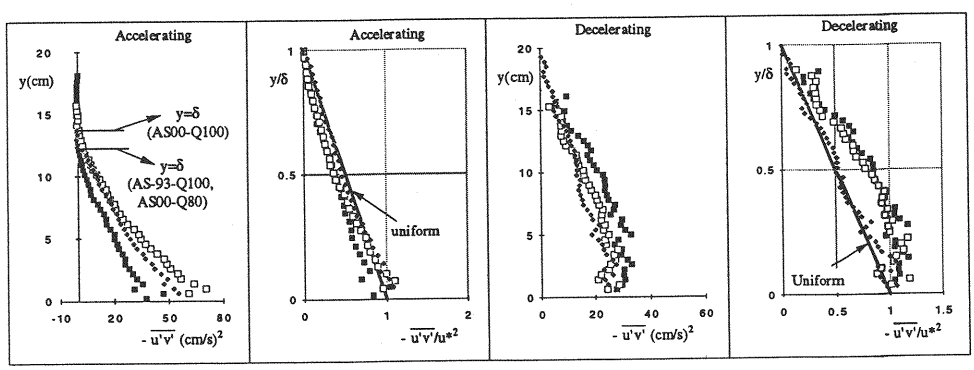

Fig. 15 Reynolds-stress profiles in non-uniform flow (for legend see Fig. 13)

Mixing Length and Eddy Viscosity

Turbulent mixing is parameterized by the turbulent eddy (mixing) viscosity, υ_t, or the mixing length, ℓ, given by:

$$\tau(y) = \rho\, \upsilon_t \frac{\partial \bar{u}}{\partial y} \qquad \tau(y) = \rho\, \ell^2 \left(\frac{\partial \bar{u}}{\partial y}\right)^2 \tag{22}$$

where, $\tau(y)$ is the Reynolds stress and $\partial\bar{u}/\partial y$ is the vertical velocity gradient. The measured velocity and Reynolds-stress profiles are used to calculate the eddy viscosity, υ_t, and the mixing length, ℓ. From plotting all the present runs (16), it is concluded that the mixing-length distribution for non-uniform flow is similar to one for uniform flow; that is to say that within the experiment range, we cannot distinguish a difference.

The two selected extreme runs have been selected to show a possible effect of flow non-uniformity. From Fig. 16 an overall tendency is evident: the dimensionless eddy viscosity is smaller for accelerating flow (mixing is damped), and larger for decelerating flow (mixing is amplified) when compared with uniform flow. This tendency is reversed in the zone close to the water surface. It is also noted that in both accelerating and decelerating flows, the dimensionless mixing length is essentially the same one as in uniform flow. The Prandtl hypothesis, $\ell = \kappa y$, is valid for small distances, independent of the type of flow.

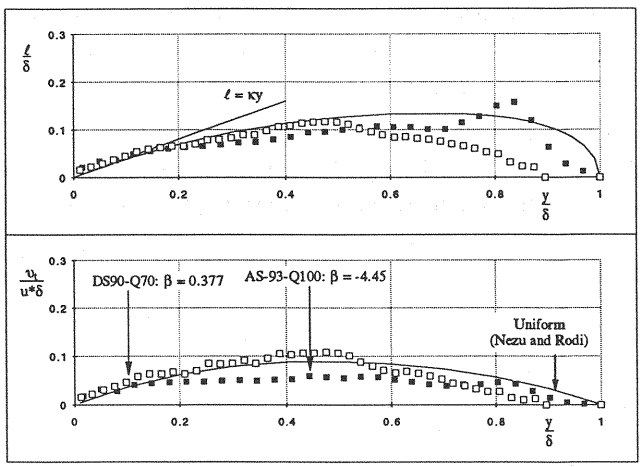

Fig. 16 Mixing-length and eddy-viscosity distributions in non-uniform flow

THEORETICAL CONSIDERATION

Above, the turbulence characteristics of non-uniform flow were discussed using the measured data. However, measurements of velocity and of turbulence profiles are a very difficult task. In the

following, we will try to develop relations with which the friction velocity, u^*_c, the vertical velocity distribution, $\overline{v}(y)$, and the Reynolds-stress profile, $\tau(y)$, in *non-uniform flow* can be calculated by using hydraulic parameters such as water depth, D, and its variation along the flow, dD/dx, and the flow discharge, Q. All these parameters are rather easy to measure.

Friction Velocity

In steady open-channel flow, the St. Venant equation of motion can be written as follows:

$$\frac{U}{g}\frac{dU}{dx} + \frac{dD}{dx} - S + \frac{1}{D}\frac{\tau_o}{\rho g} = 0 \qquad (23)$$

where D is the water depth; U is the average velocity; x is the axes along the bed slope, S, and τ_o is the shear stress on the bed. Rearranging Eq. 23, an expression for the friction velocity, u^*_c, is obtained:

$$u^{*2}_c = \frac{\tau_o}{\rho} = gDS - gD\left(\frac{dD}{dx} + \frac{U}{g}\frac{dU}{dx}\right) \qquad (24)$$

Using the equation of continuity for steady non-uniform flow:

$$\frac{d(UD)}{dx} = D\frac{dU}{dx} + U\frac{dD}{dx} = 0 \qquad \text{or} \qquad \frac{dU}{dx} = -\frac{U}{D}\frac{dD}{dx} \qquad (25)$$

Eq. 24 becomes:

$$u^*_c = \sqrt{gD\left[S - \frac{dD}{dx}(1 - Fr^2)\right]} \qquad (26)$$

where $Fr = U/\sqrt{gD}$ is the Froude number.

Thus the friction velocity in non-uniform flow can be calculated with Eq. 26 if S, D, dD/dx and U are given. For the present experiments, the friction velocities evaluated with Eq. 26 are summarized in Table 1. The friction velocity, u*, was earlier obtained using the Clauser method from the measured velocity profile in the inner region. A comparison between these two methods is possible; this is shown in Fig. 17. It is found that in the range of the present investigation, the two friction velocities agree reasonably well with each other.

Furthermore, a polynomial-regression fit to the measured Reynolds-stress profiles allows also calculation of the friction velocity, designated as u^*_τ. These results are listed in Table 1. It is noted that the three differently calculated friction velocities, u*, u^*_c and u^*_τ, agree with each other reasonably well. The difference amongst them is about 5% for all runs of accelerating flows and for most of decelerating flows. This agreement can also be used to justify the assumptions of the equivalent sand roughness, $k_s \equiv d_{50}$, and the reference-bed level, $y_o = 0.25k_s$, in Clauser's method for the evaluation of the friction velocity, u*.

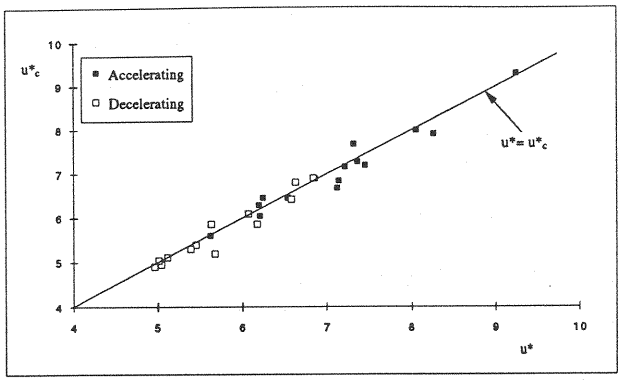

Fig. 17 Comparison of the friction velocity, using the Clause method, u*, and using St. Venant's equation, u^*_c

Vertical Velocity Distribution

For the equilibrium flows, the horizontal point velocity can be written as:

$$\bar{u}(y=y) = UF(\frac{y}{D}) \tag{27}$$

and after differentiation one obtains:

$$\frac{\partial \bar{u}}{\partial x} = F(\frac{y}{D})\frac{dU}{dx} - U\frac{dF(\frac{y}{D})}{d(\frac{y}{D})}\frac{y}{D^2}\frac{dD}{dx} \tag{28}$$

Substitution of Eq. 28 into the equation of continuity, Eq. 19 gives:

$$\frac{\partial \bar{v}}{\partial y} = -\frac{\partial \bar{u}}{\partial x} = -F(\frac{y}{D})\frac{dU}{dx} + U\frac{dF(\frac{y}{D})}{d(\frac{y}{D})}\frac{y}{D^2}\frac{dD}{dx} \tag{29}$$

Integrating Eq. 29, replacing the integration variable y by another symbol $\tilde{y}$ to distinguish from the limitation variable, and using the boundary condition of $\bar{v}$ (y=0) = 0, one obtains (16):

$$\bar{v}(y=y) = -\int_0^y F(\frac{\tilde{y}}{D})\frac{dU}{dx}d\tilde{y} + \int_0^y U\frac{dF(\frac{\tilde{y}}{D})}{d(\frac{\tilde{y}}{D})}\frac{\tilde{y}}{D^2}\frac{dD}{dx}d\tilde{y} \tag{30}$$

$$= -\frac{1}{D}\left(D\frac{dU}{dx} + U\frac{dD}{dx}\right)\int_0^y F(\frac{\tilde{y}}{D})\,d\tilde{y} + \frac{y}{D}\frac{dD}{dx}UF(\frac{y}{D})$$

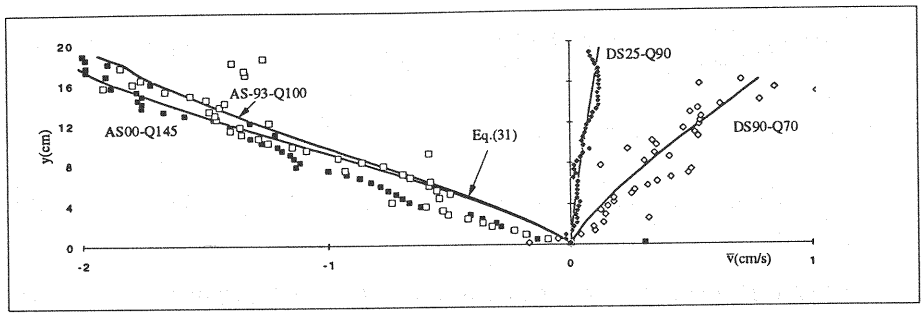

Fig. 18 Comparison of the measured and calculated, Eq. (31), vertical velocity profiles

Since the first term - containing the flow continuity equation, Eq. 25 -, vanishes, only the second term, - utilizing Eq. 27 - remains and one obtains:

$$\bar{v}(y=y) = \frac{y}{D}\frac{dD}{dx}\bar{u}(y=y) \tag{31}$$

The measured vertical velocity profiles for the selected runs are compared with Eq. 31 in Fig. 18. Agreement is reasonably good, when one realize the difficulty in measuring the small value of the velocity $\bar{v}$.

Reynolds-stress distribution

The Reynolds equation of motion and the continuity equation for two-dimensional, steady non-uniform open-channel flow can be written as follows:

$$\bar{u}\frac{\partial \bar{u}}{\partial x} + \bar{v}\frac{\partial \bar{u}}{\partial y} = -\frac{1}{\rho}\frac{dp^*}{dx} + \frac{1}{\rho}\frac{\partial \tau}{\partial y} \tag{32}$$

$$\frac{\partial \bar{u}}{\partial x} + \frac{\partial \bar{v}}{\partial y} = 0 \tag{19}$$

where $\bar{u}$ is the longitudinal point velocity; $\bar{v}$ is the vertical point velocity; τ is the Reynolds stress; p^* is the piezometric pressure whose gradient is given as:

$$\frac{dp^*}{dx} = -g\rho\left(S - \frac{dD}{dx}\right) \tag{33}$$

By using Eqs. 27 and 29, the vertical distribution of the shear stress in non-uniform open-channel flow can be deduced:

$$\frac{\partial \tau}{\partial y} = \rho \left(\bar{u} \frac{\partial \bar{u}}{\partial x} + \bar{v} \frac{\partial \bar{u}}{\partial y} \right) - g\rho \left(S - \frac{dD}{dx} \right) \tag{34}$$

Using the limiting conditions at the surface:

$$\tau (y=D) = 0 \qquad \text{and} \qquad \bar{v} (y = D) = \bar{u} (y = D) \frac{dD}{dx} \tag{35}$$

Replacing the integration variable y by another symbol $\tilde{y}$ to distinguish from the limitation variable, the integration of Eq. 34 renders (16):

$$\begin{aligned} \tau (y=y) &= g\rho (D - y)(S - \frac{dD}{dx}) - \rho \int_y^D \left(\bar{u}(y \to \tilde{y}) \frac{\partial \bar{u}(y \to \tilde{y})}{\partial x} + \bar{v}(y \to \tilde{y}) \frac{\partial \bar{u}(y \to \tilde{y})}{\partial \tilde{y}} \right) d\tilde{y} \\ &= g\rho (D - y)(S - \frac{dD}{dx}) - \rho \int_y^D \left(\frac{\partial \bar{u}^2(y \to \tilde{y})}{\partial x} + \frac{\partial \bar{u}(y \to \tilde{y})\, \bar{v}(y \to \tilde{y})}{\partial \tilde{y}} \right) d\tilde{y} \\ &= g\rho (D - y)(S - \frac{dD}{dx}) - \rho \left[\frac{\partial}{\partial x} \int_y^D \bar{u}^2(y \to \tilde{y})\, d\tilde{y} - \bar{u}(y=y)\, \bar{v}(y=y) \right] \end{aligned} \tag{36}$$

where $y \to \tilde{y}$ means that y is replaced by $\tilde{y}$. Thus it is shown that the shear-stress distribution, $\tau(y = y)$, in non-uniform flow can be calculated with Eq. 36, if the horizontal and vertical velocity profiles along the distance are measured. As this is very difficult to do, another procedure is followed.

It is supposed that the horizontal velocity distribution can be expressed by a power law such as (it should be noted here that the log-law, Eq. 16, would make a integration too difficult):

$$\frac{\bar{u}}{U} = \frac{1+m}{m} \left(\frac{y}{D} \right)^{\frac{1}{m}} \tag{37}$$

m is given by the following expression (17) when the bed is plane:

$$\frac{1}{m} = \frac{1}{4.7} \left(\frac{d_s}{D} \right)^{0.06} \tag{38}$$

In the present study, $d_s = 1.23$ cm and $13.1 \le D[\text{cm}] \le 20.5$; therefore, $5.42 \le m \le 5.56$ with an average value of $m \cong 5.5$. The integral in Eq. 36 can now be evaluated (16), using Eq. 37:

$$\frac{\partial}{\partial x} \int_y^D \bar{u}^2(y \to \tilde{y})\, d\tilde{y} = U^2 \frac{dD}{dx} \frac{(m+1)^2}{m(m+2)} \left[-1 + \frac{2(m+1)}{m} \left(\frac{y}{D} \right)^{\frac{2+m}{m}} \right]$$

Furthermore, we express, using Eqs. 31 and 35 :

$$\overline{u}(y=y)\overline{v}(y=y) = U^2 \frac{dD}{dx}\left[\frac{(m+1)^2}{m^2}\right] \left(\frac{y}{D}\right)^{\frac{m+2}{m}}$$

After institution of above expressions into Eq. 36 , one obtains:

$$\tau\,(y=y\,) = g\rho\,(D - y\,)(S - \frac{dD}{dx}) + \rho\,U^2 \frac{dD}{dx}\left[\frac{(m+1)^2}{m\,(m+2)}\right]\left[1 - \left(\frac{y}{D}\right)^{\frac{2+m}{m}}\right] \qquad (39)$$

The distribution of the Reynolds stress, $\tau(y)$, can now be calculated with Eq. 39. Known must be for a given section at x: (*i*) the slope, S, and the roughness, $m(k_s)$, of the bed, (*ii*) the flow depth, D, and the depth variation, dD/dx (both measured with the ultrasonic limnimeters) and (*iii*) the cross-sectional (average) velocity, U = Q/(DB) (measured with the electromagnetic flow meter).

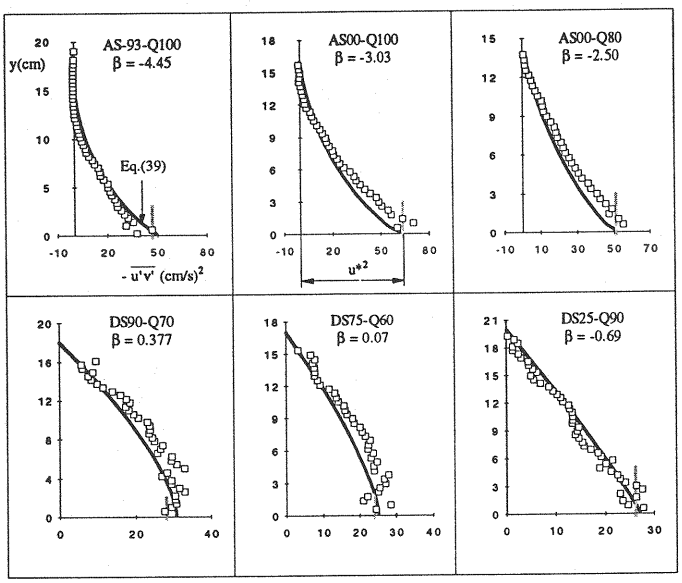

Fig. 19 Comparison of the measured and calculated, Eq. 39, Reynolds-stress profiles

In Fig. 19 the calculated Reynolds-stress profiles, $\tau(y)/\rho = -\overline{u'v'}$, are compared with the measured ones for the six selected runs (including the most accelerating and the most decelerating flows). The measured Reynolds-stress profiles in decelerating flow coincide reasonably well with the calculated ones; for accelerating flow, there exist small differences, which are possibly due the use of the power-law, Eq. 37 , being not so suitable for accelerating flows (see Fig. 5).

Furthermore, Eq. 39 can be also used to determine the shear stress on the bed, τ_o, by using the boundary condition, $\overline{v}\,(y = 0) = 0$, such as:

$$\tau_o = \tau(y=0) = g\rho D(S - \frac{dD}{dx}) + \rho U^2 \frac{dD}{dx}\left[\frac{(m+1)^2}{m(m+2)}\right] = g\rho D\left[S - (1 - \beta_B Fr^2)\frac{dD}{dx}\right] \quad (40)$$

where $\beta_B = \frac{(1+m)^2}{m(m+2)}$ is the Boussinesq coefficient. Taking $m \cong 5.5$, we have $\beta_B = 1.024$; this value agrees with a measured one (16). If we compare Eq. 40 with Eq. 26, the only difference is that in Eq. 26 this coefficient is taken as $\beta_B = 1$, an hypothesis in the St. Venant equation.

Using the definition of the pressure-gradient parameter, β, given with Eq. 13, in Eq. 39, the distribution of Reynolds stress can be written in dimensionless form as (16):

$$\frac{\tau(y)}{\tau_o} = 1 + \beta\frac{y}{D} - \frac{\rho}{\tau_0} U^2 \frac{dD}{dx}\left[\frac{(m+1)^2}{m(m+2)}\right]\left(\frac{y}{D}\right)^{\frac{m+2}{m}} \quad (41)$$

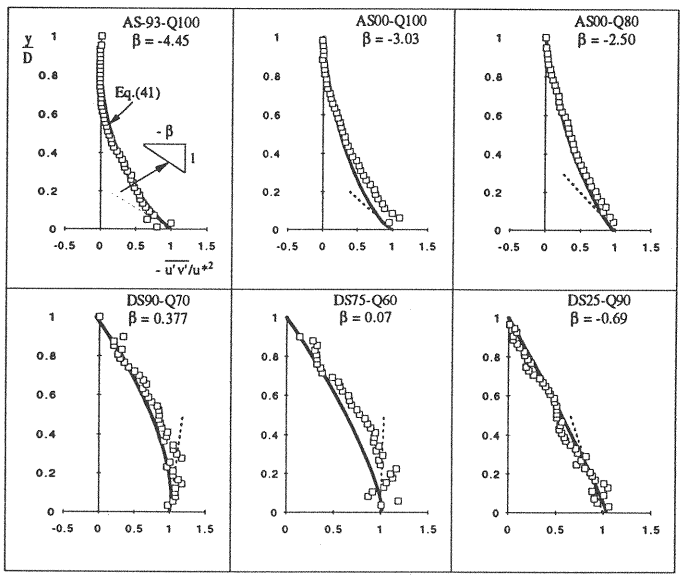

Fig. 20 Dimensionless Reynolds-stress distribution

Dimensionless Reynolds-stress profiles calculated with Eq. 41 are shown in Fig. 20, where there are also plotted the measured ones for the six selected runs. It should be noted that the τ_0-values used in Eq. 41 are the ones obtained with Eq. 40 (or Eq. 26), $\tau_o = \rho u^*_c$. The measured data have been made dimensionless using the friction velocity, u*, obtained from the measured velocity profiles in the inner region (Clauser's method). Agreement between the measured and the calculated Reynolds-stress profiles in Fig. 20 is considered to be reasonably good.

Differentiating Eq. 41, one obtains:

$$\frac{\partial\left[\frac{\tau(y)}{\tau_o}\right]}{\partial(\frac{y}{D})} = \beta - \frac{\rho}{\tau_o} U^2 \frac{dD}{dx}\left[\frac{(m+1)^2}{m^2}\right](\frac{y}{D})^{\frac{2}{m}} \tag{42}$$

This equation, evaluated for $y \rightarrow 0$, very close to the bed, gives:

$$\frac{\partial\left[\frac{\tau(y\rightarrow 0)}{\tau_o}\right]}{\partial(\frac{y}{D})} = \beta \tag{43}$$

The β-values for the respective runs are also shown in Fig. 20, as a dashed line.

SUMMARY AND CONCLUSION

The turbulence characteristics of steady non-uniform flow in a channel with rough bed have been experimentally studied using an Acoustic Doppler Velocity Profiler (ADVP). The following conclusions may be drawn:

1. The pressure-gradient parameter, β, proposed by Kironoto and Graf (8) can be well used to characterize the non-uniform open-channel flows; however the flow must be in equilibrium (Figs. 3 and 4).

2. The horizontal mean-velocity profiles, $\overline{u}(y)$, are fuller in accelerating flow and more slender in decelerating flow than the one in uniform flow (Fig. 5).

3. The log-law remains valid in the inner region (Fig. 7). The integration constant, $B_r = 8.28 \pm 0.47$, is almost independent of the β-value (Fig. 8). The Coles' wake law is valid over the entire region; the wake-strength parameter, Π, depends on the β-value and the aspect ratio, B/D (Fig. 9).

4. The vertical point velocities, $\overline{v}$, are much smaller than the horizontal ones in both accelerating and decelerating flow (Fig. 10). The tendency of their distributions is explained with the continuity equation.

5. Turbulence-intensity distributions (Fig. 13) and Reynolds-stress distributions (Fig. 15) depend also on the β-value; they decrease in accelerating and increase in decelerating flow, if compared to the ones in uniform flow.

6. The distribution of the mixing length (Fig. 16) is essentially the same as the one for uniform flow.

7. Based upon the equations of St. Venant and the Reynolds equation, formulas for estimating the friction velocity, Eq. 26, the vertical velocity, Eq. 31, and the Reynolds-stress profiles, Eq. 39 or Eq. 41, are deduced. The theoretical formulas are verified with the experimental data (Figs. 17, 18, 19 and 20).

8. The present study and its conclusion are a further evidence of the extreme utility and precision of the non-intrusive direct ADVP-measuring device.

REFERENCES

1. Bradshaw, P. : The turbulence structure of equilibrium boundary layer, J. Fluid Mech., 29(4), 625 - 645, 1967.
2. Cardoso, A.H., W.H. Graf and G. Gust : Steady gradually accelerating flow in a smooth open channel, J. of Hydr. Res., 29(4), 603 - 616, 1991.
3. Chien, N. and Wan Z. : *Mechanics of Sediment Movement* (In Chinese), Science press, Beijing, China, 1985.
4. Coleman, H. W., R. J. Moffat and W. M. Kays : The accelerated fully rough turbulent boundary layer, J. Fluid Mech., 82(3), 507 - 528, 1977.
5. Graf, W. H. and M. Altinakar : *Hydraulique Fluviale* (Tome 1), Presses Polytechniques et Universitaires Romandes, Lausanne, Switzerland, 1993.
6. Graf, W. H. and L. Suszka : Sediment transport in steep channel, J. Hydrosience and Hydr. Eng., Jap. SCE, 5(1), 11-26, 1987.
7. Herring, H. J. and J. F. Norbury : Some experiments on equilibrium boundary layer in favorable pressure gradient, J. Fluid Mech., 27(3), 541 - 549, 1967.
8. Kironoto, B. and W. H. Graf : Turbulence characteristics in rough non-uniform open-channel flow, (Submitted for publication), 1995.
9. Lhermitte, R. and R. Serafin : Pulse-to-pulse coherent doppler signal processing techniques, J. Atmos. Oce. Tech., 4, 293-308, 1984.
10. Lhermitte, R. and U. Lemmin : Open-Channel flow and turbulence measurement by high resolution Doppler ADVP, Ann. Rep. LRH. B24, Ecole Polytechnique Fédérale, Lausanne, Switzerland, 1990.
11. Lhermitte, R. and U. Lemmin : Turbulent flow microstructures observed by Sonar, Geophysical Research Letter, 20(9), 823-826, 1993.
12. Lhermitte, R. and U. Lemmin : Open-Channel flow and turbulence measurement by high resolution Doppler ADVP, (Accepted for publication), 1994.
13. Nezu, I. and W. Rodi : Open channel flow measurement with a Laser Doppler anemometer, J. Hydr. Eng., ASCE, 112(5), 335-355, 1986.
14. Rotta, J. C. : *Turbulente Stroemungen*, B. G. Teubner Verlag, Stuttgart, Germany, 1972.
15. Song, T., W.H. Graf and U. Lemmin : Uniform flow in steep open channels with gravel Bed, (Submitted for publication), 1995.
16. Song, T. : Turbulence in open-channel flows with gravel beds, Doctoral dissertation (in preparation), Ecole Polytechnique Fédérale, Lausanne, Switzerland, 1995
17. Tang, C. : Threshold of sediment (in Chinese), Chinese J. Hydr. Eng., No.2, Beijing, 1963.
18. Tsujimoto, T., A. Saito and K. Nitta : Open-channel flow with spatial acceleration or deceleration, KHL Progress Report , Hydr. Lab., Kanazawa University, Japan, 1990.

NOTATION

The following symbols are used in this paper:

B	= flume width (60 cm);
B/D	= aspect ratio;
B_r	= constant of integration of the log-law;
d_{50}	= medium diameter of gravel;
D	= water depth;
dD/dx	= variation of the water depth;
$Fr = U/\sqrt{gD}$	= Froude number;
g	= gravitational acceleration;
k_s	= roughness;
ℓ	= mixing length;
m	= constant in the power law;
p^*	= piezometric pressure;
Q	= flow discharge;
$R_e = 4DU/\upsilon$	= Reynolds number;
S	= bed slope;
$U = Q/DB$	= cross-sectional average velocity;
U_C	= maximum point velocity;
u^*	= friction velocity obtained with Clauser method;
u^*_τ	= friction velocity from the measured Reynolds-stress profile;
u^*_c	= friction velocity calculated with the St. Venant equation;
u, v	= instantaneous velocities in horizontal and vertical direction;
$\overline{u}, \overline{v}, \overline{V_j}$	= mean values of u, v, V_j;
u', v', V_j'	= fluctuation components of u, v, V_j;
V_j	= instantaneous radial velocity which the transducer "sees";
$\overline{V_j'^2}$, $\overline{u'^2}$, $\overline{v'^2}$ and $\overline{u'v'}$	=variances and covariance of the corresponding velocity fluctuations;
x	= horizontal distance (measured along the bed slope);
y	= vertical distance (measured from the gravel top);
$y_o = (-)\ 0.25k_s$	= reference bed level;
α_i	= angles between transducer beam and vertical direction;
β	= dimensionless pressure-gradient parameter for open channel flow;
δ	= distance between the gravel bed and the point where $\overline{u} = U_c$;
Π	= Coles' wake parameter;
ρ	= density of water;
τ_o	= bed-shear stress;
$\tau(y)$	= Reynolds-shear stress;
υ	= kinematic viscosity of water;
υ_t	= eddy viscosity.

(Received February 3, 1994 : revised May 9, 1994)